Journal of ELECTRONIC MATERIALS, Vol. 47, No. 3, 2018
https://doi.org/10.1007/s11664-017-6048-x

Microstructural Investigation, Raman and Magnetic Studies on Chemically Synthesized Nanocrystalline Ni-Doped Gadolinium Oxide ($Gd_{1.90}Ni_{0.10}O_{3-\delta}$)

B.J. SARKAR,[1] J. MANDAL,[1] M. DALAL,[1] A. BANDYOPADHYAY,[1,2] B. SATPATI,[3] and P.K. CHAKRABARTI[1,4]

1.—Solid State Research Laboratory, Department of Physics, Burdwan University, Burdwan, W.B. 713 104, India. 2.—Department of Physics, University of Gour Banga, Mokdumpur, Malda, W.B. 732103, India. 3.—Surface Physics and Material Science Division, Saha Institute of Nuclear Physics, Kolkata, W.B. 700 064, India. 4.—e-mail: pabitra_c@hotmail.com

Nanocrystalline Ni-doped gadolinium oxide ($Gd_{1.90}Ni_{0.10}O_{3-\delta}$, GNO) is synthesized by co-precipitation method. The as-prepared sample is annealed in vacuum at 700°C for 6 h. Analyses of the x-ray diffractogram by Rietveld refinement method, transmission electron microscopy and Raman spectroscopy of GNO recorded at room temperature confirmed the pure crystallographic phase and complete substitution of Ni-ions in Gd_2O_3 lattice. Magnetization (M) as a function of temperature (T) and magnetic field (H) is measured by a superconducting quantum interference device magnetometer, which suggests the presence of ferromagnetic/antiferromagnetic phases together with a paramagnetic phase. From the M–T curve it can be shown that the ferromagnetic phase dominates over para-/antiferromagnetic phases in the temperature range of 300–100 K, but from 100 K to 50 K, the antiferromagnetic phase dominates over ferro-/paramagnetic phases. Hysteresis loops recorded at different temperatures indicate the presence of weak ferro-/antiferromagnetism, which dominates in the low field region ($\sim$ 4000 Oe), above which magnetization increases linearly. The sharp increase of magnetization in M–T curve observed in the temperature range of 50–5 K confirms the presence of dominating ferromagnetic plus paramagnetic phase over antiferromagnetic part. For the first time a combined formula generated from three-dimensional (3D) spin wave model and Johnston formula is proposed to analyze the coexistence of different magnetic phases in different temperature ranges. Interestingly, the combined formula successfully explains the co-existence of different magnetic phases along with their contribution at different temperatures. The onset of ferromagnetism in $Gd_{1.90}Ni_{0.10}O_{3-\delta}$ is explained by oxygen vacancy mediated F-centre exchange (FCE) coupling mechanism.

Key words: Nanoparticle, chemical synthesis, magnetic materials, magnetic properties

INTRODUCTION

Dilute magnetic semiconductors (DMSs) have drawn considerable attention due to their advanced technological applications in spintronics since the last decade.[1,2] In the family of DMS systems, room temperature ferromagnetism (RTFM) in transition metal (TM) ion-doped ZnO, SnO_2, TiO_2, CeO_2 etc.[3–8] have been observed by various researchers. In addition, dilute magnetic dielectrics (DMDs) are also an important area of research due to their enhanced magnetic property at room temperature

(Received August 3, 2017; accepted December 27, 2017; published online January 9, 2018)

(RT) and high dielectric constant. Recently it has been found that TM ion doped rare earth (RE) oxide exhibits the property of DMD[7–10] with high dielectric constant,[11] as well as high value of magnetization compared to that of DMS due to high free ion magnetic moment of RE ions (R^{3+}). Because of high resistivity, high dielectric constant and large band gap, rare earth oxides are the potential candidate for new generation spin filter, magnetic sensor and storage devices.[12] In recent times, the magnetic behavior of TM ion doped rare earth oxides such as $Dy_{1.90}Co_{0.10}O_3$,[13] $Eu_{1.90}Fe_{0.10}O_{3-\delta}$,[14] $Sm_{1.90}Fe_{0.10}O_3$,[15] $Sm_{1.9}Co_{0.1}O_3$,[16] $Gd_{1.90}Co_{0.10}O_{3-\delta}$,[17] $Gd_{1.90}Fe_{0.10}O_{3-\delta}$[18] and $Tb_{1.90}Ni_{0.10}O_3$[19] were reported. Petoral et al. investigated the magnetic properties of 5% Tb doped Gd_2O_3.[20] So far as these authors' knowledge, no report of magnetic ordering was observed in Ni-doped Gd_2O_3 till now. Considering the importance of rare earth oxides, particularly Gd_2O_3 as Gd^{3+} is S-state ion with high value of free ion magnetic moment ($\sim 7.94\ \mu_B$) and dielectric constant[11] and in continuation of our earlier work, here we report the preparation, structural refinement, morphology, Raman spectroscopy and magnetic behavior of Ni^{2+} ion doped gadolinium oxide with composition $Gd_{1.90}Ni_{0.10}O_{3-\delta}$ (GNO) where the percentage of doping is same with results of previous studies. In this manuscript we have investigated the magnetic behavior of $Gd_{1.90}Ni_{0.10}O_{3-\delta}$ and compared the magnetic properties with available results of $Gd_{1.90}Co_{0.10}O_{3-\delta}$,[17] $Gd_{1.90}Fe_{0.10}O_{3-\delta}$[18] and 5% Tb doped Gd_2O_3[20] where the percentage of doping is same. The crystallographic phase of GNO and the substitution of Ni^{2+}-ions in the Gd_2O_3 host lattice are confirmed after analyzing the x-ray diffractogram by Rietveld refinement. Analyses of transmission electron microscopy (TEM) and Raman observation of the sample also confirmed the absence of any impurity phase in the sample. Weak ferromagnetic ordering is observed in GNO at RT in the low field region (at an applied field of ~ 4000 Oe) above which the magnetization increases linearly with the applied field indicating the strong paramagnetic behavior of GNO. In the high field region ($\sim 5\ T$) the paramagnetic behavior of Gd_2O_3 dominates over ferromagnetic/antiferromagnetic behavior of the sample due to high magnetic moment of the host cations. The onset of ferromagnetism (FM) in GNO are successfully explained by oxygen vacancy mediated FM or so-called F-centre exchange (FCE) coupling mechanism.[21] In FCE mechanism an electron is trapped in oxygen vacancy which acts as a coupling centre, through which doped magnetic ions align in ferromagnetic order.

EXPERIMENTAL METHODS

Synthesis of $Gd_{1.90}Ni_{0.10}O_{3-\delta}$

The precursor materials for the preparation of nanocrystalline GNO in simple co-precipitation method were gadolinium oxide, Gd_2O_3 (Alfa Aesar, 99.9% purity) and nickel chloride hexahydrate, $NiCl_2{\cdot}6H_2O$ (Sigma Aldrich, 99.9% purity). To prepare $Gd_{1.90}Ni_{0.10}O_{3-\delta}$ by co-precipitation method, first required amount of gadolinium oxide was taken in a beaker and few drops of de-ionized water were added in the gadolinium oxide to obtain the slurry. Few drops of concentrated hydrochloric acid (HCl) were added in the slurry to obtain a clear solution of gadolinium chloride ($GdCl_3$). The freshly prepared solution of $GdCl_3$ was slowly heated at 60°C for duration of ~ 3 h to remove the extra amount of HCl and finally micro-crystals of $GdCl_3$ were obtained. The micro-crystals of $GdCl_3$ were dissolved in 100 mL of triple distilled boiled water and sonicated for half an hour. In another beaker required amount of nickel chloride was taken and 100 mL of triple distilled boiled water was added to obtain the nickel chloride solution and sonicated for half an hour. To obtain a clear homogeneous chloride solution, the solution of gadolinium chloride and nickel chloride were taken in a beaker and 200 mL of triple distilled boiled water was added to it and sonicated for 1 h. In a beaker sodium hydroxide (NaOH) pellets were dissolved in triple distilled water to obtain a diluted sodium hydroxide solution. To obtain the co-precipitation, this newly prepared diluted sodium hydroxide solution was added drop wise in the chloride solution until the pH of the solution was maintained at ~ 9 and as a result the desired gadolinium hydroxide $Gd(OH)_3$ was precipitated. The co-precipitated particles were washed several times by triple distilled boiled water to neutralize the pH of the solution and to remove extra ions. Finally, the co-precipitated particles were filtered by vacuum filtration technique and were dried at RT. The as-dried sample was annealed at 700°C for 6 h in vacuum to obtain the desired crystallographic phase and to enhance the oxygen vacancy in the doped sample, which is helpful to obtain magnetic ordering in GNO. Boiling condition was maintained during co-precipitation to lower the adsorbed oxygen in the water that may helpful to enhance the oxygen vacancy in the sample.

Materials Characterization

The x-ray diffraction (XRD) pattern of GNO was recorded using a Brukers Advanced D8 diffractometer with Cu K_α radiation ($\lambda = 1.54184$ Å) in the 2θ range from 20° to 75°. Transmission electron microscopy (TEM) of GNO was recorded using FEI, Tecnai G^2 F30-ST microscope operated at 300 kV. The same microscope is equipped with a scanning unit, a high-angle annular dark field (HAADF) detector for scanning transmission electron microscopy (STEM-HAADF) and the energy dispersive x-ray spectroscopy (EDS, EDAX Inc.) attachment to perform elemental analyses. Raman spectra of GNO were recorded at RT in the wave number range of 70–800 cm^{-1} using a T64000

Raman Spectrophotometer (J. Y. HORIBA). An incident radiation of wavelength 632 nm emitted from He-Ne Laser was used as the exciting radiation in Raman spectrometer that interfaced with the computer in the photon counting mode. Static magnetic measurements viz., M versus T curve under field cooled (FC) and zero field cooled (ZFC) conditions, magnetization versus field (M–H) curves were carried out at different temperatures from 300 K down to 5 K by using Quantum design SQUID magnetometer.

RESULTS, ANALYSIS AND DISCUSSION

XRD and Rietveld Analysis

The x-ray diffractogram of GNO is shown in Fig. 1. The positions of 2θ and relative intensities of diffraction peaks in the XRD pattern of GNO are in good agreement with the cubic structure of Gd_2O_3 having space group $Ia\bar{3}$ and are assigned according to JCPDS file No. 43-1014. The average crystallite size of the sample is calculated from the line broadening of the 100% intense peak (222) in the (XRD) pattern by using the Debye–Scherrer equation

$$\langle D\rangle = 0.89\lambda/(\beta_{1/2}\cos\theta)$$

where $\langle D\rangle$ is the average crystallite size, λ is the wavelength of the incident x-ray radiation and θ is the corresponding Bragg angle. Here, $\beta_{1/2}$ is the full-width at half-maximum (FWHM) of the (222) peak. The average crystallite size of GNO estimated using Scherrer equation is 17 ($\pm$1) nm which indicates the nanocrystalline nature of the sample. To derive the structural (lattice parameters, unit cell volume etc.) and microstructural (coherent domain size/crystallite size, micro-strain etc.) parameters, Rietveld analysis of XRD pattern was carried out with the help of a software MAUD.[22] During the analysis of XRD data, each profile was fitted with a pseudo-Voigt function and all the parameters related to structure/microstructure were considered as refinable parameters. The good fitting is also assessed from the value of goodness of fit (GOF) and the reliability parameters, namely R_w (weighted profile factor), R_{exp}, (expected weighted profile factor), and R_b (the Bragg factor) defined as[17–19]

$$R_w = \left[\frac{\sum w_i(I_{io}-I_{ic})^2}{\sum w_i I_{io}^2}\right]^{1/2} \quad (1)$$

$$R_{exp} = \left[\frac{N-P}{\sum w_i I_{io}^2}\right] \quad (2)$$

$$R_b = \frac{\sum |I_{ko}-I_{kc}|}{\sum I_{ko}} \quad (3)$$

$$GOF = \frac{R_w}{R_{exp}} \quad (4)$$

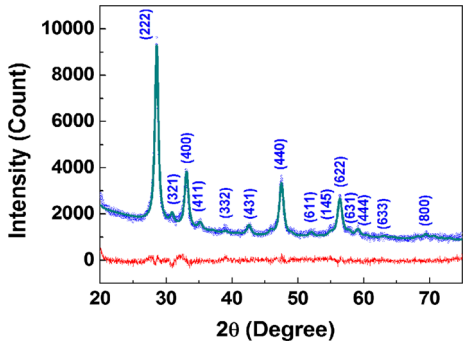

Fig. 1. X-ray diffractograms and the fitted pattern of $Gd_{1.90}Ni_{0.10}O_{3-\delta}$ obtained from the Rietveld analysis.

Here I_{io} and I_{ic} represent the observed and calculated intensities at the ith step, I_k represent the intensity assigned to the kth Bragg reflection at the end of the refinement cycles; $w_i = (1/I_{io})$ is the weight factor. N is the total number of points, which are considered in the refinement and P denotes the number of parameters refined. For the best fitted pattern the value of GOF is around unity. Rietveld analysis also confirms the cubic structure of GNO with space group $Ia\bar{3}$ and the value of lattice parameter obtained from Rietveld analysis is a = 10.8325 Å ($\pm$ 6 $\times$ 10^{-3}) with GOF $\sim$ 1.32. The value of GOF (very close to 1) indicates that the observed pattern is well fitted by the derived pattern in the Rietveld refinement. The absence of extra peak due to any probable impurity phase like Ni or NiO clusters in the observed pattern confirmed the formation of pure crystallographic phase of GNO. The average nanocrystallite size estimated from Rietveld refinement of XRD pattern of GNO is $\sim$ 19 ($\pm$ 0.5) nm. During Rietveld refinement of XRD pattern of GNO we consider a mixture of Gd_2O_3 and NiO phase and with the progression of refinement iterations it is observed that the volume fraction of NiO phase diminishes gradually and ultimately become zero. This fact ruled out the formation of NiO phase in the sample. To find out the role of oxygen vacancy on the introduction of ferromagnetism in GNO, the oxygen occupancy was also estimated during Rietveld analysis and the corresponding value of oxygen occupancy is $\sim$ 0.897, which yields the formula unit of GNO to be ($Gd_{1.90}Ni_{0.10}O_{3-\delta}$) with δ = 0.309. The results of Rietveld refinement of the sample are summarized in Table I. From the Rietveld analysis bond lengths obtained in GNO are: O1-Gd1: 2.51 Å, O1-Gd2: 2.31 Å, O1-Gd2: 2.39 Å, O1-Gd2: 2.44 Å while for undoped Gd_2O_3[23] bond lengths are: O1-Gd1: 2.33 Å, O1-Gd2: 2.26 Å, O1-Gd2: 2.32 Å, O1-Gd2: 2.38 Å respectively.

TEM Analysis

To study the morphology of nanocrystalline GNO, TEM observations were carried out. Some low

magnification micrographs, selected area electron diffraction (SAED) patterns and lattice fringe pattern of GNO recorded during high resolution TEM (HRTEM) observations are shown in Fig. 2a, b, c, and d. From the micrographs (Fig. 2a and b) it is seen that the particles are agglomerated. We could not measure the average particle size of GNO from TEM micrograph due to high agglomeration of the nanoparticles. Most of the nanoparticles have a dumbbell-like shape. The SAED pattern of GNO is shown in Fig. 2c. The different lattice planes corresponding to Gd_2O_3 were identified by calculating the diameters of the different rings in the SAED pattern and are also assigned in Fig. 2c. The lattice fringe pattern of GNO is displayed in Fig. 2d. The separation between the consecutive parallel planes is calculated and the calculated value is 3.12 Å which corresponds to the lattice plane (222) of Gd_2O_3, which is assigned and marked in Fig. 2d. From Fig. 2c and d it is seen that no lattice planes other than Gd_2O_3 are observed. Thus, TEM study also ruled out the presence of any impurity phase in the sample of GNO, which confirms the complete substitution of Ni^{2+}-ions in the lattice of Gd_2O_3. This observation is in good agreement with the results obtained from Rietveld analysis of XRD pattern.

Table I. Results from Rietveld analysis of the sample $Gd_{1.90}Ni_{0.10}O_{3-\delta}$ (GNO)

Cell (Å)	a: 10.8325 ($\pm$ 6 $\times$ 10^{-3})
Strain	1.05 $\times$ 10^{-5} ($\pm$ 1 $\times$ 10^{-3})
Size (nm)	19 ($\pm$ 0.5)
R_w (%)	1.95
R_b (%)	1.52
R_{exp} (%)	1.48
GOF	1.32

To investigate the chemical compositions of GNO, STEM-HAADF-EDX analysis was performed and the presence of Gd, Ni and O is confirmed. Figure 3a shows EDX spectra of GNO. The trace of Cu and C are appeared in the spectrum as we have used a carbon coated Cu grid in TEM observation. No traces of any impurity elements have been observed in EDX spectra, which establish the purity of the sample GNO. We have determined the weight percentages of Ni and Gd in $Gd_{1.90}Ni_{0.10}O_{3-\delta}$ from EDX measurement and the respective values are 4.72% and 95.28%, respectively. These values are quite close with our chosen stoichiometry of 5% and 95%. STEM-HAADF image (Fig. 3b) indicates that Gd and Ni are uniformly distributed in the doped sample. Also, there is no trace of Ni or NiO clusters in the sample. This is also in good agreement with

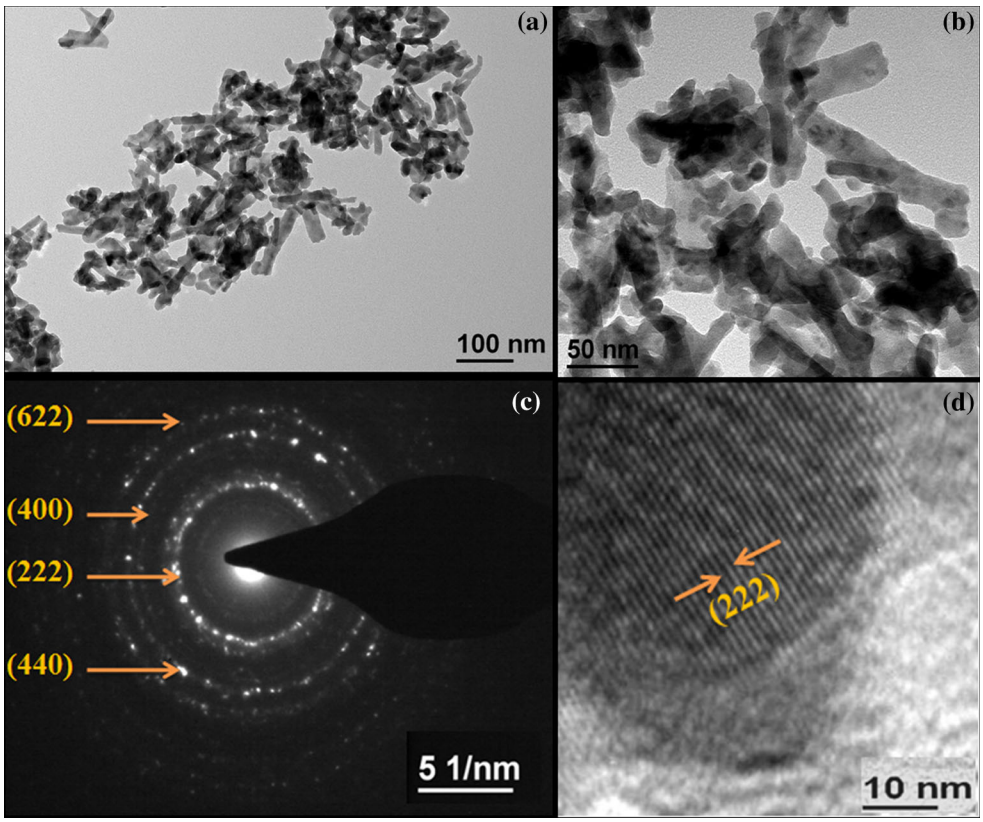

Fig. 2. Results of HRTEM observations of $Gd_{1.90}Ni_{0.10}O_{3-\delta}$ (a) and (b) HRTEM micrographs (c) SAED pattern and (d) lattice fringe pattern.

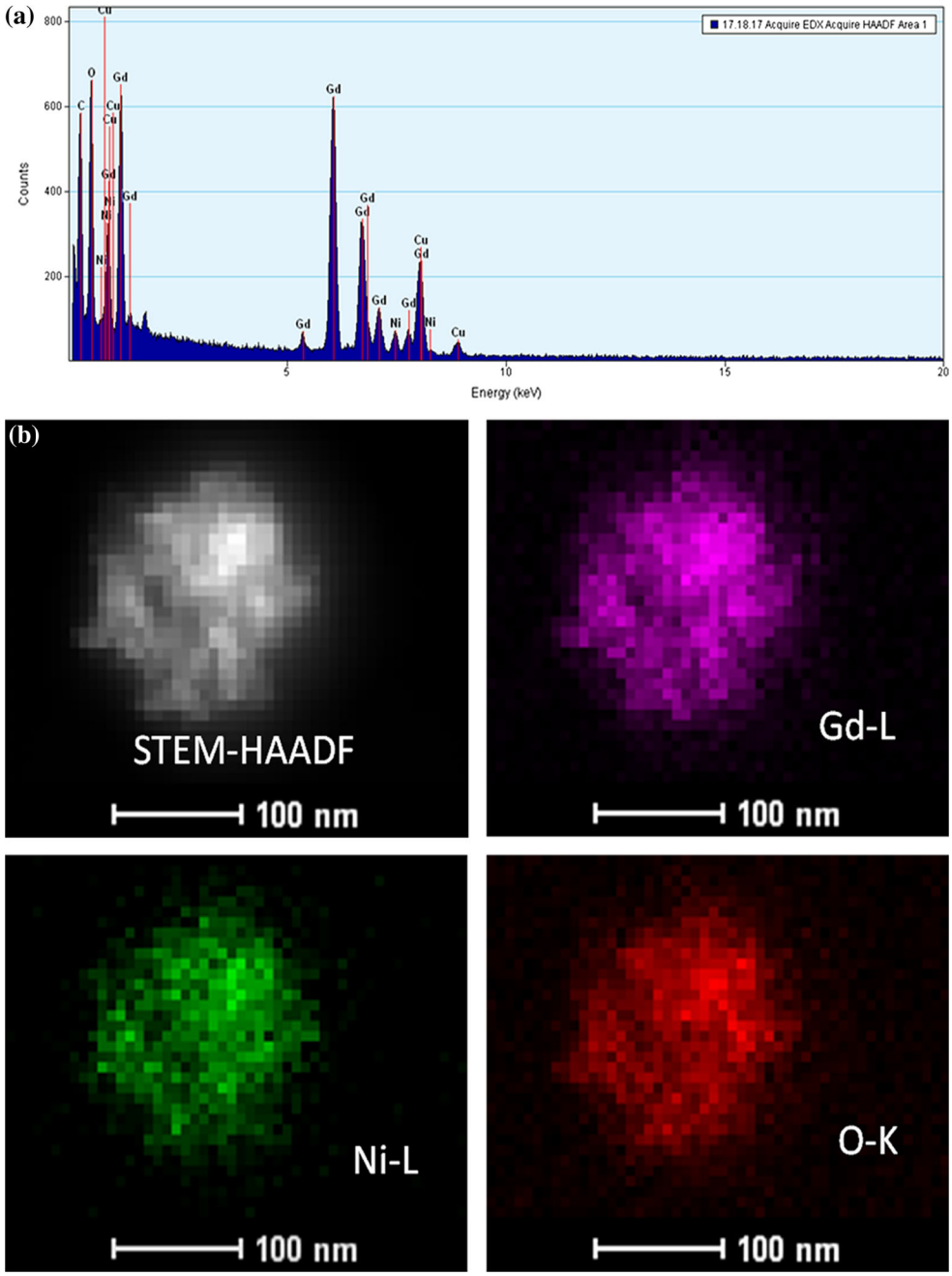

Fig. 3. (a) Energy dispersive x-ray (EDX) spectra of $Gd_{1.90}Ni_{0.10}O_{3-\delta}$, (b) STEM-HAADF image.

the results obtained from Rietveld analysis and Raman spectroscopy.

Raman Spectroscopy

Raman active phonon modes generated in Raman spectra are the characteristics of different features like crystallographic phase, presence of impurity, structural defects etc. Generally, Gd_2O_3 exists in both cubic (*C*-type) and monoclinic (*B*-type) structures. Luyer et al.[24] studied experimentally and theoretically the Raman spectroscopy of Gd_2O_3 in both cubic and monoclinic phases. Zarembowitch et al.[25] performed experimentally the Raman spectroscopy of monoclinic *B*-type structure. Rietveld analysis of the XRD pattern confirms cubic structure of GNO with space group $Ia\bar{3}$. Raman-active modes in cubic Gd_2O_3 has been predicted by Bloor and Dean using the factor group analysis.[26] Using the factor group theory, the number of distinct Raman active phonon modes in cubic phase of rare earth oxide are 22 and the possible modes are $4E_g$, $4A_g$, $14F_g$, $5E_u$, $5A_u$, and $16F_u$[26] where all the

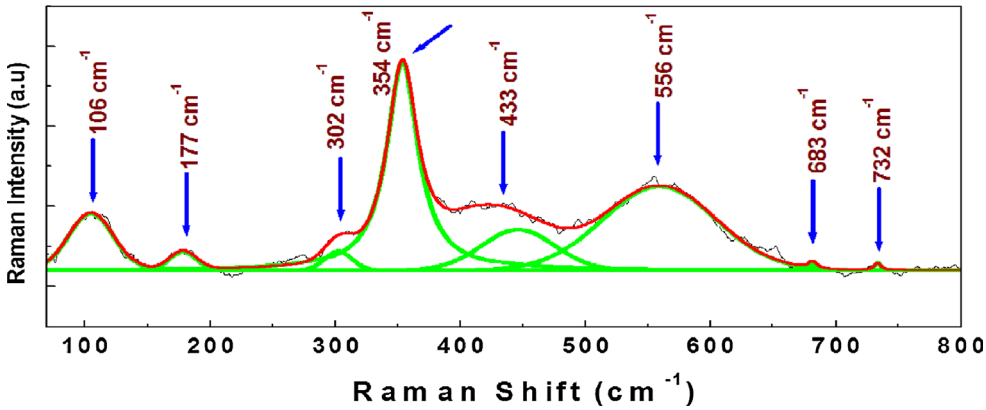

Fig. 4. Room temperature Raman Spectra of $Gd_{1.90}Ni_{0.10}O_{3-\delta}$ observed in the wave number range of 70–800 cm^{-1}.

Table II. Results extracted from the observed Raman spectra of $Gd_{1.90}Ni_{0.10}O_{3-\delta}$ at room temperature

Raman band position (cm^{-1}) obtained from cubic *C* type structure of Gd_2O_3 (Ref. 22)	Raman band position (cm^{-1}) obtained from $Gd_{1.90}Fe_{0.10}O_{3-\delta}$ (Ref. 18)	Raman band position (cm^{1}) obtained from $Gd_{1.90}Co_{0.10}O_{3-\delta}$ (Ref. 17)	Raman band position (cm^{-1}) obtained from $Gd_{1.90}Ni_{0.10}O_{3-\delta}$
81m	–	66	–
85vw	–	–	–
95s	–	91	–
108vw	102	–	106
119s	–	111	–
135w	–	–	–
145w	144	–	–
198w	185	–	177
235w	–	–	–
299vw	257	–	–
316m	314	–	302
337vw	–	–	–
361vs	354	339	354
401w	–	–	–
413vw	–	–	–
435sh	418	–	433
447m	–	–	–
479vw	–	–	–
568m	562	552	556
	656	–	683
	–	–	732

vw very weak, *w* weak, *m* medium, *s* strong, *vs* very strong, *sh* shoulder.

gerade (g) modes are Raman active, E_u and A_u modes are Raman inactive and F_u modes are infrared active.[26] In the observed Raman spectra of GNO recorded at RT, Raman active modes are located in the region between 70 cm^{-1} and 800 cm^{-1} which are shown in Fig. 4. Here, eight prominent Raman peaks are observed for the cubic phase of the doped sample located at 106 cm^{-1}, 177 cm^{-1}, 302 cm^{-1}, 354 cm^{-1}, 433 cm^{-1}, 556 cm^{-1}, 683 cm^{-1}, and 732 cm^{-1}. The absence of the characteristic boson peak near $\sim$ 90 cm^{-1} corresponding to amorphous phase of Gd_2O_3 indicating the well crystallinity of the sample GNO and amorphous phase is totally disappeared in GNO.[27] From Fig. 4 it is clear that the strongest Raman peak of cubic Gd_2O_3 is observed at 354 cm^{-1}. Garcia-Murillo et al. studied the Raman spectra of 5% Eu^{3+} doped Gd_2O_3 where the Raman active modes were located at 93 cm^{-1}, 117 cm^{-1}, 313 cm^{-1}, 359 cm^{-1}, 442 cm^{-1}, and 565 cm^{-1}.[27] Raman spectroscopy of Co doped Gd_2O_3 ($Gd_{1.90}Co_{0.10}O_{3-\delta}$) and Fe doped Gd_2O_3 ($Gd_{1.90}Fe_{0.10}O_{3-\delta}$) are also reported in our previous works.[17,18] The wave numbers of the corresponding Raman peaks for doped and undoped Gd_2O_3 in the

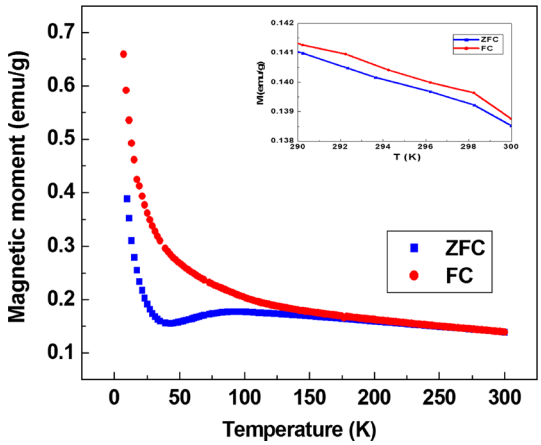

Fig. 5. Thermal variation of ZFC and FC magnetizations of $Gd_{1.90}Ni_{0.10}O_{3-\delta}$. Inset is the enlarged view of ZFC and FC magnetizations in the temperature range of 300–290 K.

cubic phase are shown in Table II. The absence of a Raman mode corresponding to the Ni cluster and nickel-oxide[28] in the observed Raman spectra of GNO indicates the absence of these phases in the sample, which is consistent with Rietveld refinement of the XRD pattern and TEM observations of GNO. Because of the doping of Ni-ions in the cubic Gd_2O_3 lattice, Raman modes are slightly shifted from undoped Gd_2O_3 suggests that the dominant fraction of Ni gets incorporated substitutionally into the Gd_2O_3 lattice and forms GNO. There are many reasons for the shift of Raman modes, such as oxygen vacancies within the material, disorder induced defects or phonon confinement effects etc.[29] Zhang et al.[30] suggested that oxygen vacancies play a crucial role for shifting and broadening of Raman modes. The change of bond length and bond energy may be correlated with the shift of Raman modes. The shift of Raman active modes in GNO towards lower wave number region compared to

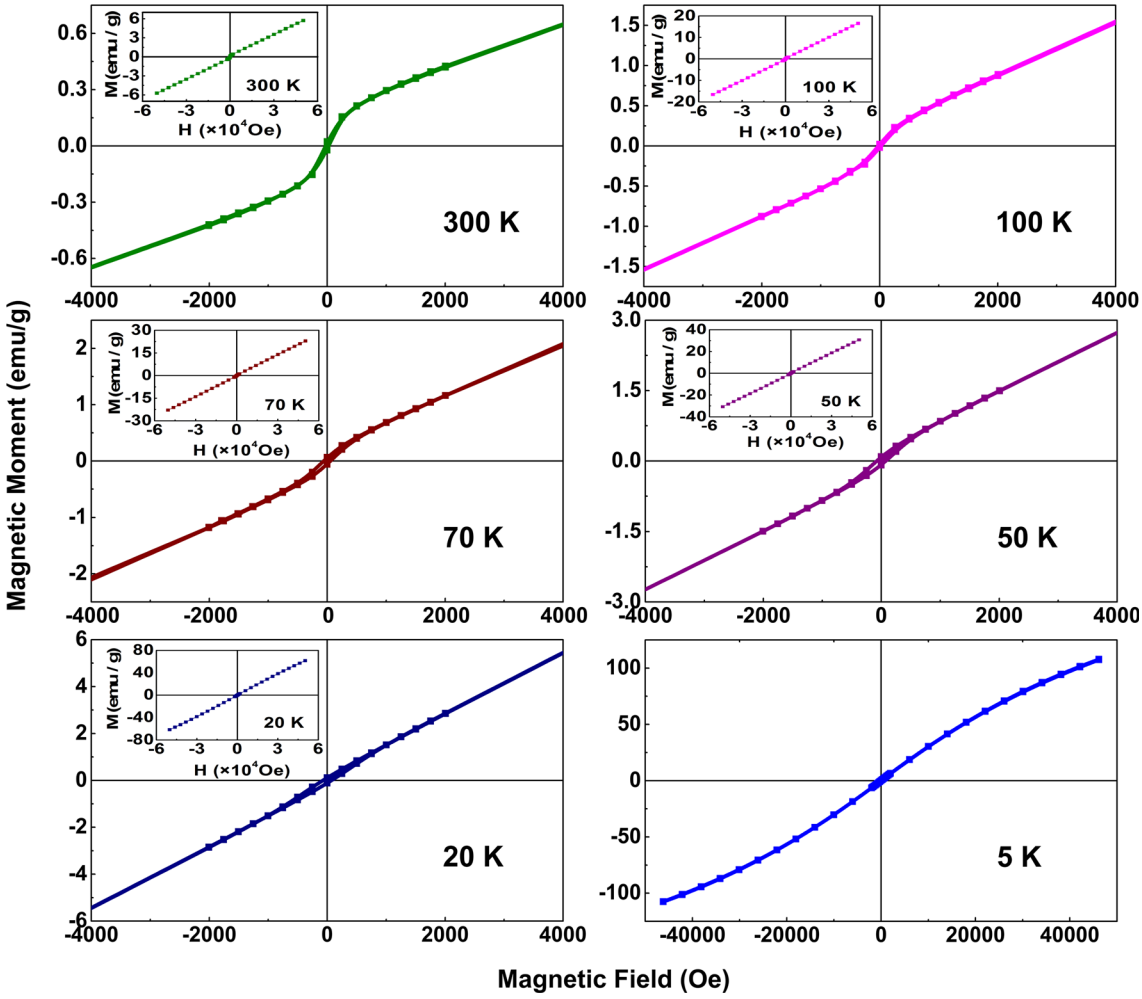

Fig. 6. Magnetic hysteresis (M-H) loops of the sample $Gd_{1.90}Ni_{0.10}O_{3-\delta}$ recorded at temperatures 300 K, 100 K, 70 K, 50 K, 20 K, and 5 K. Insets are the loops in the full region of the applied field ($\sim$ 5 *T*).

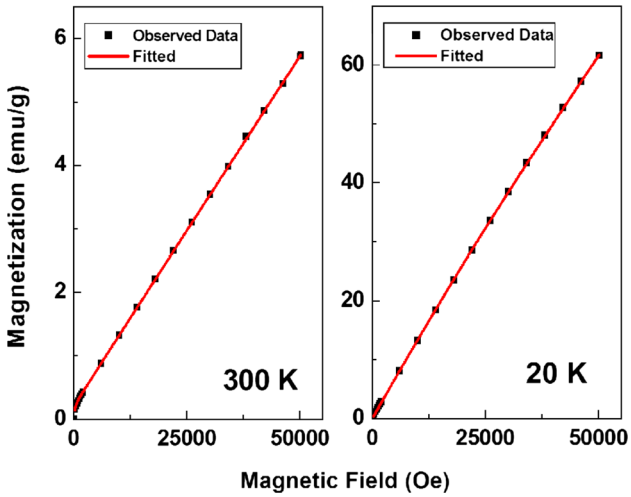

Fig. 7. Initial magnetization of the M–H curve recorded at 300 K and 20 K along with the fitted data using modified Langevin function. Symbols: observed data, Solid Line: fitted by modified Langevin function.

undoped Gd_2O_3 may be attributed to the increase in bond length in GNO and presence of oxygen vacancies in the sample, which is also in good agreement with the results obtained from Rietveld analysis.

Magnetic Properties

Figure 5 shows the M–T curves of GNO under zero field cooled (ZFC) and field cooled (FC) conditions. To measure FC magnetization, the sample was cooled from 300 K down to 5 K with an applied field of 200 Oe. It is apparent that FC and ZFC curves are overlapped down to ~ 220 K, but the enlarged view shows that FC and ZFC magnetization values are different from 300 K, which is shown in the inset of Fig. 5, implying that there is no superparamagnetic effect at and below ~ 300 K. From M–T curve it is seen that ZFC magnetization increases slowly with the lowering of temperature from ~ 300 K down to ~ 100 K. But below ~ 100 K down to ~ 50 K, magnetization decreases with the lowering of temperature and attains a minimum value of ~ 0.157 emu/g at ~ 50 K, and below this temperature down to ~ 5 K magnetization increases rapidly with the lowering of temperature. The sharp rise in magnetization below ~ 50 K is the characteristic of DMS/DMD material, which is due to the uncoupled or weakly coupled TM ions. To confirm the presence of magnetic ordering in GNO, M–H loops were recorded with maximum applied field of ~ 5 *T*. Some selected M–H loops recorded at 300 K, 100 K, 70 K, 50 K, 20 K, and 5 K are displayed in Fig. 6. The M–H loop of GNO recorded at RT is a clear hysteresis loop in the low field region (at an applied field of ~ 4000 Oe) and the extracted values of coercivity, remanence and maximum magnetization are ~ 25 Oe, 0.016 emu/g and 5.8 emu/g, respectively. In case of GNO, hysteresis loops are prominent in the low field region (~ 4000 Oe) which is evident from Fig. 6, but when the loops are shown in the full region of the applied field (~ 5 *T*) the behavior looks like paramagnetic type. We have tried to fit the observed unsaturated M–H curve using the modified Langevin function. The modified Langevin function is expressed as

$$M = M_S[\coth(\mu H/K_B T) - (K_B T/\mu H)] + KH$$

The symbols have their usual meanings.[15] The initial magnetization of the M–H curve at 300 K and 20 K along with the Langevin fitting is shown in Fig. 7.

To find the dominating magnetic phase and to explain the onset of nonlinearity in the low field region (~ 4000 Oe) even at RT of GNO, we have proposed a combined formula generated from 3D spin wave model and Johnston formula, which includes the term for paramagnetic, ferromagnetic and antiferromagnetic to fit the M–T curve in the ZFC condition. According to this, combined formula[17–19,31] becomes

$$M(T) = \frac{CH}{T} + \frac{C_{AF}H}{T + T_N} + M(0)(1 - AT^{3/2}) + C_{0C}$$

The first term in the equation is for the paramagnetic part of the host, the second term is the antiferromagnetic contribution, the third term indicates the ferromagnetic contribution arising from the 3D spin wave model and the fourth term is the temperature independent contribution to magnetization. In the previous equation $M(0)$ is the saturation magnetization at $T = 0$ K due to the ferromagnetic component, and A is a coefficient correlated to the structural properties of the material. The good fitting of the M–T curve in ZFC condition using the combined formula is shown in Fig. 8, which indicates that magnetization in the full range of temperatures under the ZFC condition is successfully explained by the combined formula. The individual contribution of ferromagnetic, paramagnetic and antiferromagnetic parts at some temperatures such as 300 K, 200 K, 150 K, 100 K, 80 K, and 50 K obtained from the fitting of M–T data under the ZFC condition using the combined formula generated from the 3D spin wave model and Johnston formula are given in Table III. The extracted values of magnetization from fitting the M–T data indicates that in region-1 (300–100 K) the ferromagnetic contribution dominates over the other two counterparts in the low field region and the fitting parameters are $M(0)$ = 0.158 emu/g, C = 0.003 emu K/g Oe, C_{AF} = 0.067 emu K/g Oe, respectively. But in the high field region, the paramagnetic behavior of the sample dominates over ferromagnetic behavior due to the high magnetic moment of the host cations. In region-2 (100–50 K) of M–T curve it is seen that below ~ 100 K down to ~ 50 K the decrease of magnetization with lowering of temperature may be due to the

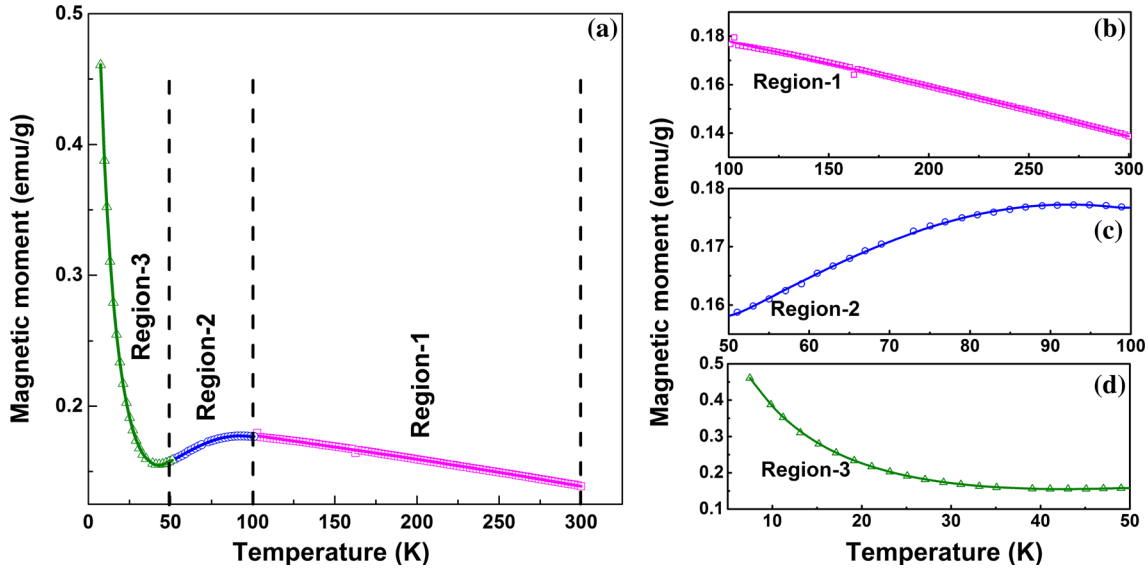

Fig. 8. Zero field cooled magnetization versus temperature curve of $Gd_{1.90}Ni_{0.10}O_{3-\delta}$ fitted with combined 3D spin wave model and Johnston formula in the temperature range of (a) 300–5 K, (b) 300–100 K, (c) 100–50 K and (d) 50–5 K.

Table III. Contribution of different magnetic phases extracted from the observed magnetization versus temperature curve of $Gd_{1.90}Ni_{0.10}O_{3-\delta}$ using the combined formula

Temperature (K)	Observed magnetization value (emu/g)	Magnetization due to ferromagnetic contribution (emu/g)	Magnetization due to paramagnetic contribution (emu/g)	Magnetization due to antiferromagnetic contribution (emu/g)
300	0.138	0.117	0.002	0.019
200	0.16	0.136	0.003	0.019
150	0.17	0.143	0.004	0.02
100	0.176	0.006	0.042	0.123
80	0.175	0.005	0.052	0.137
50	0.16	0.088	0.06	0.004

dominating presence of antiferromagnetic ordering over paramagnetism of the host cations and ferromagnetic ordering in the sample. The presence of an antiferromagnetic phase together with ferromagnetic plus paramagnetic phases is confirmed from the extracted values of the individual magnetization obtained from the fitting of M–T data and the fitting parameters are $M(0) = 5 \times 10^{-4}$ emu/g, $C = 0.021$ emu K/g Oe, $C_{AF} = 0.12$ emu K/g Oe, respectively. Thus, due to the strong antiferromagnetic contribution, the antiferromagnetic phase dominates over paramagnetic plus ferromagnetic phases in region-2. In the M–T curve there is a broad maximum at temperature $T_{max} \sim 95$ K and a point of inflection at ~ 50 K. According to Bonner and Fisher, this behavior is the characteristics of the antiferromagnetic chain[19,31] and the antiferromagnetic exchange interaction follows the relation

$$\frac{K_B T_{max}}{J} = 1.282$$

The estimated value of antiferromagnetic exchange interaction $\frac{J}{K_B} = 74$ K.

In region-3 (50–5 K) the large value of the ferromagnetic contribution and small value of the antiferromagnetic contribution indicates that in this region the ferromagnetic phase dominates over the antiferromagnetic phase, indicating that ZFC magnetization increases rapidly with lowering of temperature. But due to the strong paramagnetic contribution of the host cations, the loops are not saturated. The lack of saturation in the loops demonstrates that a large fraction of nanoparticles are in paramagnetic phase. In region-3 the fitting parameters are $M(0) = 0.06$ emu/g, $C = 0.015$ emu K/g Oe, $C_{AF} = 0.001$ emu K/g Oe, respectively. Actually, in the first phase of the fitting we have tried to fit the magnetic data into the entire temperature region using one set of parameters, namely, $M(0)$, C etc. But here it seen that the values of $M(0)$ and C in three different regions change due to the change of domination of different magnetic

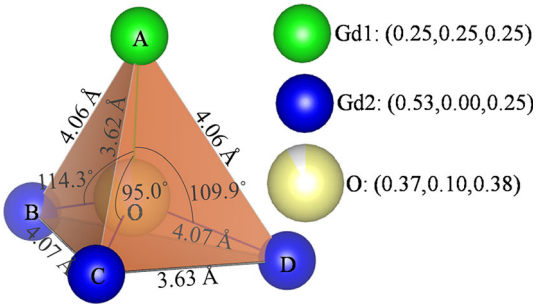

Fig. 9. Atomic structure and bond angles of $Gd_{1.90}Ni_{0.10}O_{3-\delta}$ derived from MAUD.

phases, and accordingly, the magnetic data in the whole region are fitted quite satisfactorily. The paramagnetic contribution comes from the strong exchange interaction among the spins of Gd^{3+} unpaired electrons.[32] The presence of hysteresis loops in the low field region is due to the presence of ferromagnetic/antiferromagnetic ordering in the sample and the unsaturated M–H loop is the signature of the presence of paramagnetism. A canonical antiferromagnet does not exhibit any sort of hysteresis loop, but for nanoscaled antiferromagnets hysteresis can be observed.[19] The introduction of magnetic ordering due to impurities can be easily ruled out by Rietveld analysis of the XRD pattern, TEM and Raman analysis of GNO. Alhough different mechanisms can explain the observed magnetic ordering in the TM-ion doped DMS/DMD system, the proper explanation of the onset of magnetic ordering is yet to be explored. As the concentration of magnetic cations responsible for the ordering is low, i.e. the Ni cations, the observed magnetic ordering cannot be explained by the carrier mediated Ruderman–Kittel–Kasuya–Yosida (RKKY) magnetic exchange mechanism reported by Hou et al.[33] The RKKY interaction is based on the concentration of free carrier, but at such a low doping Gd_2O_3 cannot transform into a metal. Coey et al.,[21] reported the oxygen vacancy mediated ferromagnetism, which is related to the formation of bound magnetic polarons. Among different possibilities, the most plausible explanation for the present case is the defect/oxygen vacancy mediated F centre exchange (FCE) coupling mechanism, as the sample is annealed in vacuum and the formation of oxygen vacancy in the sample can be substantiated by the Rietveld analysis of GNO. In FCE mechanism, an electron trapped in an oxygen vacancy (Vo) forms the F-centre, and the trapped electron occupies an orbital, which overlaps the *d* shell of neighboring Ni ions. The magnetic exchange interactions between V_O and Ni ions align most of the spins of Ni ions around V_O, constitutes BMPs. The magnetic behavior of doped diluted magnetic semiconductors is characterized by the interaction between large collective spins which are known as bound magnetic polarons (BMPs).[34] According to the Hund's rule and Pauli Exclusion Principle, spin orientations of the trapped electrons and the neighbouring Ni ions should be parallel in order to achieve ferromagnetic ordering.[35] Moreover, the doping of Ni^{2+} ions may enhance the number of oxygen vacancies in doped Gd_2O_3 to maintain charge neutrality in the system. Antiferromagnetism in GNO appears mainly due to the presence of strong super-exchange interaction of Gd^{3+}-$O^{2-}$$Gd^{3+}$ and Ni^{2+}-$O^{2-}$$Ni^{2+}$.[32] According to FCE mechanism the direct exchange interaction between two Ni ions through oxygen vacancy is ferromagnetic in nature which leads to the alignment of the spin of the magnetic atom.[21,32,36] The concentration of BMPs at relatively high temperature is quite low[17,18] and only few Ni ions are ferromagnetically coupled through oxygen vacancies which contribute weak ferromagnetic ordering in the sample.[32] With the lowering of temperature the decrease in thermal randomization of magnetic spins and the increase of FCE interaction mediated by oxygen vacancy due to increase of BMP concentration favours the dominance of FM phase in GNO and thus strengthens the ferromagnetic exchange interaction at lower temperature.[21,32,36] Again with the lowering of temperature both polaron size and total intrapolaron exchange energy increase logarithmically and probability of overlapping of BMPs and interactions between BMPs increases, which leads to the prominent long range FM ordering in the sample at low temperature.[34,37] According to BMP model, the coupling between two Ni^{2+} ions through oxygen vacancy (Ni^{2+}-$O_{vacancy}$-Ni^{2+}) is ferromagnetic in nature.[32] In our case, only a few Ni^{2+} ions underwent coupling with the $O_{vacancy}$ at high temperature. In addition, Gd^{3+}-$O^{2-}$$Gd^{3+}$ and Ni^{2+}-$O^{2-}$$Ni^{2+}$ antiferromagnetic super exchange interaction are also present. Therefore, the presence of the Gd^{3+}-$O^{2-}$$Gd^{3+}$ and Ni^{2+}-$O^{2-}$$Ni^{2+}$ antiferromagnetic super exchange interaction in addition to the diluted Ni^{2+}-$O_{vacancy}$-Ni^{2+} ferromagnetic exchange interaction, magnetization of the Ni-doped Gd_2O_3 samples show ferromagnetic/antiferromagnetic behavior at different temperatures. In addition, paramagnetic behavior due to host cations and ferromagnetic ordering due to FCE interactions, the onset of antiferromagnetic ordering based on superexchange interactions and bond angles can also be explained with the help of atomic structure of GNO derived from MAUD which is shown in Fig. 9. Ni^{2+} ions are mostly found in the position (0.25, 0.25, 0.25), i.e., in the position of Gd1. No Ni^{2+} ions are found in the position of Gd^{3+} ions i.e. Gd2: (0.53, 0.00, 0.25). The bond lengths among Gd1 and Gd2 are AB=4.06 Å, AC=3.62 Å, AD=4.06 Å and the bond angles are ∠AOB=114.3°, ∠AOC=95.0°, ∠AOD=109.9°. Correspondingly, the bond lengths among Gd2 are BC=4.07 Å, CD=3.63 Å, BD=4.07 Å and the bond angles are ∠BOC=119.6°, ∠COD=97.3°, ∠BOD=117.5°. The strength of exchange interaction is maximum when the bond angle is 180° and in this

case the two spins (spins of Gd1 and Gd2) become antiparallel. The strength becomes weaker as the bond angle becomes smaller.[38] Thus, here the superexchange interactions responsible for the onset of antiferromagnetic ordering in GNO could be the interactions between the Gd^{3+} ions at A and B (A–B: 4.06 Å, ∠AOB=114.3°), A and D (A–D: 4.06 Å, ∠AOD=109.9°), B and C (B–C: 4.07 Å, ∠BOC=119.6°), B and D (B-D: 4.07 Å, ∠BOD=117.5°). Also, 5% Ni substitution is found in the position of Gd1. Thus, the superexchange interactions A-B and A-D with Ni^{2+} ions at A-position and Gd^{3+} ions at B- and D-positions contribute to the onset of antiferromagnetism in GNO.

Compared to other previously reported work on doped Gd_2O_3, room temperature ferromagnetism is first observed in GNO. In our previous works on Co doped Gd_2O_3[17] and Fe doped Gd_2O_3[18] paramagnetic to ferromagnetic phase transition was observed at ~ 20 K. Petoral et al.[20] investigated the magnetic behavior of 5% Tb doped Gd_2O_3 where hysteretic behavior appeared at 5 K. Thus, it is revealed that oxygen vacancy plays a key role in the magnetic behavior of GNO formed by vacuum annealing and charge neutrality in the system. In our earlier works, Co doped Gd_2O_3 ($Gd_{1.90}Co_{0.10}O_{3-\delta}$)[17] exhibits paramagnetic nature with maximum magnetization at ~ 300 K around 5.6 emu/g at 5 *T*, Fe doped Gd_2O_3 ($Gd_{1.90}Fe_{0.10}O_{3-\delta}$)[18] exhibits paramagnetic nature with maximum magnetization at 300 K around 5.7 emu/g with a maximum applied field of ~ 5 *T*. Hazarika et al.[39] reported the superparamagnetic behavior of Gd_2O_3 nanorod at 300 K with maximum magnetization ~ 6 emu/g at 6 *T*. Patel et al.[32] reported that the paramagnetic behavior with feeble antiferromagnetic contribution in Co doped Gd_2O_3 nanorod with maximum magnetization at 300 K was ~ 0.06 emu/g with a maximum applied field of ~ 2 *T*. But in the present system, we have investigated the magnetic properties of Ni doped Gd_2O_3 ($Gd_{1.90}Ni_{0.10}O_{3-\delta}$), where room temperature ferromagnetism is observed in the low field region (~ 4000 Oe), but with maximum applied field of ~ 5 T dominant paramagnetic behavior with maximum magnetization at 300 K is ~ 5.8 emu/g is found. The formation of oxygen vacancy to maintain charge neutrality in GNO plays a key role for the enhancement of magnetization compared to Co and Fe doped Gd_2O_3. Also, the huge enhancement in the magnetization of GNO compared to that of 5% Tb doped Gd_2O_3[20] may be attributed to the presence of oxygen vacancy, which is achieved not only by annealing the sample in vacuum, but also from charge neutrality. In the case of the Co/Fe doped Gd_2O_3 system the situation may be different from that of Ni doped systems. The enhancement of magnetization normally depends on dopants as well as on the vacancies. The probability of existence of different valence states of Co/Fe (+ 2, + 3 and so on valence states) is more plausible compared to that of Ni. Because of this the creation of an oxygen vacancy in Ni doped Gd_2O_3 is more probable than previous cases (Co/Fe doped Gd_2O_3 systems). Thus, for the first time we have reported the room temperature ferromagnetism in a doped Gd_2O_3 system. Thus, it is revealed that the increase of FCE interaction mediated by oxygen vacancies in GNO describes the enhanced magnetization compared to other doped or undoped Gd_2O_3 reported so far.

CONCLUSION

Nanocrystalline samples of $Gd_{1.90}Ni_{0.10}O_{3-\delta}$ are successfully prepared where the TM ions of Ni^{2+} are entered in the cubic lattice of Gd_2O_3. The oxygen vacancy is enhanced due to annealing the as-prepared sample in vacuum. The analyses of XRD, HRTEM and Raman data do not find any impurity of NiO or other, and the formation of a cluster of Ni-atoms is not found in these analyses. Different magnetic phases such as antiferromagnetic, paramagnetic and ferromagnetic are found and duly analyzed. Though different magnetic phases are found in the magnetic measurements, the dominating phase depends mainly on two factors, namely, value of the magnetic field and temperature. To know the dominating magnetic phase at a given temperature, the measured data are successfully fitted by a combined formula consisting of 3D spin wave model and the Johnston formula, and we have considered this formula for the first time. The good fitting of the magnetic data by the combined formula successfully explains the dominating magnetic phase as a function of temperature. This unique approach will be helpful to analyze any magnetic data to know the magnetic phase of the system. The dominating magnetic phase such as paramagnetic and ferromagnetic as evaluated from the analysis is explained by FCE mechanism. The present doped system with high value of magnetization would be quite interesting for applications as DMD.

ACKNOWLEDGEMENTS

The authors wish to acknowledge the financial support provided by the UGC-DAE-CSR-KC, Govt. of India (Project file No. UGC-DAE-CSR-KC/CRS/13/MS04/0814/0837 dated 16.12.2013) and the financial support provided by the DST, Govt. of India through FIST Programme (File No. SR/FST/PSI-170/2011(C) dated 18.05.2012) and UGC, Govt. of India through the CAS program. The Authors further acknowledge the UGC-DAE Consortium for Scientific Research, Kolkata Centre for providing facility to measure the magnetic property at low temperature with high magnetic field.

REFERENCES

1. M. Venkateshan, C.B. Fitzgerald, and J.M.D. Coey, *Nature* 430, 630 (2004).
2. H. Ohno, *Science* 281, 951 (1998).
3. H.S. Hsu, J.C.A. Huang, Y.H. Huang, Y.F. Liao, M.Z. Lin, C.H. Lee, J.F. Lee, S.F. Chen, L.Y. Lai, and C.P. Liu, *Appl. Phys. Lett.* 88, 242507 (2006).

4. H. Kimura, T. Fukumura, M. Kawasaki, K. Inaba, T. Hasegawa, and H. Koinuma, *Appl. Phys. Lett.* 80, 94 (2002).
5. W.K. Park, R.J. Ortega-Hertogs, J.S. Moodera, A. Punnoose, and M.S. Seehra, *J. Appl. Phys.* 91, 8093 (2002).
6. J. Chen, P. Rulis, L. Ouyang, S. Satpathy, and W.Y. Ching, *Phys. Rev. B* 74, 235207 (2006).
7. R.K. Singhal, P. Kumari, S. Kumar, S.N. Dolia, Y.T. Xing, M. Alzamora, U.P. Deshpande, T. Shripathi, and E. Saitovitch, *J. Phys. D Appl. Phys.* 44, 165002 (2011).
8. Q.Y. Wen, H.W. Zhang, Q.H. Yang, Y.Q. Song, and J.Q. Xiao, *J. Mag. Mag. Mater.* 321, 3110 (2009).
9. M.C. Prestgard, G. Siegel, Q. Ma, and A. Tiwari, *Appl. Phys. Lett.* 103, 102409 (2013).
10. J.M.D. Coey, M. Venkatesan, and C.B. Fitzgerald, *Nat. Mater.* 4, 173 (2005).
11. I.Z. Mitrovic and S. Hall, *J. Telecommun. Inf. Technol.* 4, 51 (2009).
12. J.-G. Wan, Q. Lu, B. Chen, F. Song, J.-M. Liu, J. Dong, and G. Wang, *Appl. Phys. Lett.* 95, 152901 (2009).
13. A. Bandyopadhyay, S. Sutradhar, B.J. Sarkar, A.K. Deb, and P.K. Chakrabarti, *Appl. Phys. Lett.* 100, 252411 (2012).
14. A. Bandyopadhyay, A.K. Deb, S. Kobayashi, K. Yoshimura, and P.K. Chakrabarti, *J. Alloys Compd.* 611, 324 (2014).
15. J. Mandal, B.J. Sarkar, A.K. Deb, and P.K. Chakrabarti, *J. Mag. Mag. Mater.* 371, 35 (2014).
16. N.W. Gray and A. Tiwari, *J. Appl. Phys.* 110, 033903 (2011).
17. B.J. Sarkar, A. Bandyopadhyay, J. Mandal, A.K. Deb, and P.K. Chakrabarti, *J. Alloys Compd.* 656, 339 (2016).
18. B.J. Sarkar, A.K. Deb, and P.K. Chakrabarti, *RSC Adv.* 6, 6395 (2016).
19. J. Mandal, M. Dalal, B.J. Sarkar, and P.K. Chakrabarti, *J. Electron. Mater.* (2016). https://doi.org/10.1007/s11664-016-5077-1.
20. R.M. Petoral Jr, F. Söderlind, A. Klasson, A. Suska, M.A. Fortin, N. Abrikossova, L. Selegård, P.O. Käll, M. Engström, and K. Uvdal, *J. Phys. Chem. C* 113, 6913 (2009).
21. J.M.D. Coey, A.P. Douvalis, C.B. Fitzgerald, and M. Venkatesan, *Appl. Phys. Lett.* 84, 1332 (2004).
22. L. Lutterotti, MAUD, Version 2.046 (2006). http://www.ing.unitn.it/maud/.
23. A. Bartos, K.P. Lieb, M. Uhrmacher, and D. Wiarda, *Acta Crystallogr. B* 49, 165 (1993).
24. C.L. Luyer, A. Garcia-Murillo, E. Bernstein, and J. Mugnier, *J. Raman Spectrosc.* 34, 234 (2003).
25. J. Zarembowitch, J. Gouteron, and A.M. Lejus, *J. Raman Spectrosc.* 9, 263 (1972).
26. D. Bloor and J.R. Dean, *J. Phys. C Solid State Phys.* 5, 1237 (1972).
27. A. Garcia-Murillo, C.L. Luyer, C. Garapon, C. Dujardin, E. Bernstein, C. Pedrini, and J. Mugnier, *Opt. Mater.* 19, 161 (2002).
28. N. Mironova-Ulmane, A. Kuzmin, I. Steins, J. Grabis, I. Sildos, and M. Pärs, *J. Phys: Conf. Ser.* 93, 012039 (2007).
29. B. Santara, B. Pal, and P.K. Giri, *J. Appl. Phys.* 110, 114322 (2011).
30. W.F. Zhang, Y.L. He, M.S. Zhang, Z. Yin, and Q. Chen, *J. Phys. D Appl. Phys.* 33, 912 (2000).
31. D.C. Johnston, R.K. Kremer, M. Troyer, X. Wang, A. Klümper, S.L. Bud'ko, A.F. Panchula, and P.C. Canfield, *Phys. Rev. B* 61, 9558 (2000).
32. S.K.S. Patel, P. Dhak, M.K. Kim, J.H. Lee, M. Kim, and S.K. Kim, *J. Mag. Mag. Mater.* 403, 155 (2016).
33. D.L. Hou, X.J. Ye, X.Y. Zhao, H.J. Meng, H.J. Zhou, X.L. Li, and C.M. Zhen, *J. Appl. Phys.* 102, 033905 (2007).
34. A.C. Durst, R.N. Bhatt, and P.A. Wolff, *Phys. Rev. B* 65, 235205 (2002).
35. Q.Y. Wen, H.W. Zhang, Y.Q. Song, Q.H. Yang, H. Zhu, and J.Q. Xiao, *J. Phys. Condens. Matter* 19, 246205 (2007).
36. G.W. Pratt Jr, *Phys. Rev.* 108, 1233 (1957).
37. J.Z. Cai, L. Li, S. Wang, W.Q. Zou, X.S. Wu, and F.M. Zhang, *Phys. B* 424, 42 (2013).
38. S. Chikazumi, *Physics of Ferromagnetism* (New York: Oxford University Press, 1997).
39. S. Hazarika, N. Paul, and D. Mohanta, *Bull. Mater. Sci.* 37, 789 (2014).